BIOPHYSICS

A novel method for sensor-based quantification of single/multicellular force dynamics and stiffening in 3D matrices

Bashar Emon[1], Zhengwei Li[1], Md Saddam H. Joy[1], Umnia Doha[1], Farhad Kosari[2], M. Taher A. Saif[1]*

Cells in vivo generate mechanical traction on the surrounding 3D extracellular matrix (ECM) and neighboring cells. Such traction and biochemical cues may remodel the matrix, e.g., increase stiffness, which, in turn, influences cell functions and forces. This dynamic reciprocity mediates development and tumorigenesis. Currently, there is no method available to directly quantify single-cell forces and matrix remodeling in 3D. Here, we introduce a method to fulfill this long-standing need. We developed a high-resolution microfabricated sensor that hosts a 3D cell-ECM tissue formed by self-assembly. This sensor measures cell forces and tissue stiffness and can apply mechanical stimulation to the tissue. We measured single and multicellular force dynamics of fibroblasts (3T3), human colon (FET) and lung (A549) cancer cells, and cancer-associated fibroblasts (CAF05) with 1-nN resolution. Single cells show notable force fluctuations in 3D. FET/CAF coculture system, mimicking cancer tumor microenvironment, increased tissue stiffness by three times within 24 hours.

INTRODUCTION

Cell traction is a key mediator of mechanotransduction, which helps cells maintain their size and shape, guide tissue development and homeostasis, and support various physiological and pathological processes, e.g., wound healing (*1*, *2*), fibrosis (*3*), angiogenesis (*4*), migration (*5*, *6*), and metastasis (*7*–*11*). Cell contractility creates a link between physical cues and chemical signaling, hence establishing a dynamic reciprocity (*7*, *12*–*15*) between cells and the surrounding microenvironment involving neighboring cells and the extracellular matrix (ECM). As a result, measuring traction force and assessing downstream effects, such as signaling and matrix remodeling, are very important for understanding numerous biological processes and disease progression. Methods to quantify cell traction on two-dimensional (2D) substrates have been developed and advanced over the past three decades. However, cells in vivo are in 3D environment with ECM around them. To date, there is no method to directly quantify cell traction and cell-induced matrix remodeling in 3D. This paper closes this gap by developing a unique method for direct measurement of single-cell forces and determination of matrix stiffening through remodeling in 3D ECM over time.

Cell contractility on 2D substrates was first performed using wrinkles produced by cells on silicone rubber films (*16*, *17*), but wrinkling of thin films is a nonlinear phenomenon that provides a qualitative output. Later, Wang and colleagues (*18*, *19*) developed a technique to quantify cell forces on 2D polyacrylamide (PA) substrates that allowed computation of traction stresses from substrate deformation using computational methods. This technique, referred to as traction force microscopy (TFM), was effective because of PA hydrogel being optically transparent, tunable for mechanical properties, and linearly elastic over a wide range of strains (as high as 70%) for constitutive analysis (*18*, *20*). Subsequent improvements in data collection, analysis, and rendering have made it possible to measure traction stresses with high spatial and temporal resolution (*21*–*23*). Other techniques have also been developed such as micropillar arrays (*24*–*26*) or Förster resonance energy transfer (*27*, *28*), but these methods depend on soft elastic materials as 2D substrates and are considerably more complex than TFM.

2D cell culture has provided insights into various biological processes, but cellular response and behavior in 3D environments can be very different (*29*, *30*). Quantifying forces in 3D fibrous scaffolds such as collagen is challenging (*31*) because of (i) lack of reliable mechanical characterization of the ECM at cellular scale since macroscopic mechanical properties of collagen is different from local microarchitectural properties at cellular scale and (ii) continuous local remodeling of ECM by cells. Stout and colleagues (*32*) suggested measuring the mean deformation metrics (MDMs) of collagen due to force applied by the cells. These MDMs are quantified solely by the 3D displacement field of the cell-surrounding matrices and can indicate overall shape change of the cell (e.g., contractility, mean volume change, and rotation). However, this kinematics-based method cannot provide any information about cell tractions and does not account for the ECM remodeling. Later, Steinwachs and colleagues (*33*) outlined a computational method to measure cell forces in collagen biopolymers using a finite element approach. They characterized the nonlinear mechanical properties of the biopolymers and developed a constitutive equation to compute traction from the 3D deformation field. Although promising, this method is also limited because of the difficulties in measuring accurate deformation fields, the assumptions of constitutive equations (stress-strain relations), and computationally expensive analysis. 3D tissue force was measured using microfabricated pillar structures by Legant *et al.* (*34*). However, single-cell forces or tissue remodeling could not be measured. Consequently, measurements of cellular traction and remodeling in 3D ECM still remain a challenge.

In addition to guiding cell signaling, traction forces also alter tissue stiffness that play a significant role in various natural and pathological processes such as aging, cancer, fibrosis, and cardiovascular diseases (*3*, *7*, *35*–*39*). As the cells generate traction and migrate, they also deposit collagen, cross-link fibers, and rearrange matrices, a process that is known to stiffen ECM, tissues, and tumors (*40*–*43*). As a result, similar to cell contractility, matrix remodeling is a dynamic

[1]Department of Mechanical Science and Engineering, University of Illinois at Urbana-Champaign, Urbana, IL, USA. [2]Department of Molecular Medicine, Mayo Clinic, Rochester, MN, USA.
*Corresponding author. Email: saif@illinois.edu

process that needs to be monitored with time in association with forces. To our knowledge, there is a lack of devices and/or methods that offer simultaneous measurement of cell forces and remodeling in 3D matrices.

Here, we develop an ultrasensitive sensor, integrated with a self-assembled 3D tissue construct with a single or a discrete number of cells. The sensor is microfabricated from polydimethylsiloxane (PDMS) and can measure cellular forces, circumventing the necessity of constitutive relations in analytically challenging 3D matrices. With a resolution of ~1 nN, the sensor is capable of directly quantifying single-cell forces in collagen using force equilibrium laws. In addition, the sensor can be used as an actuator to measure change in ECM stiffness due to remodeling as a function of time and to apply prescribed stretch or compression on the cell-ECM matrix to explore cell response to mechanical deformation in 3D. Hence, the sensing platform offers a range of application for biophysical investigations of cells and tissues. Here, we present the details of the sensor and the experimental results that establish novelty, applicability, and versatility.

RESULTS AND DISCUSSION

Concepts and design of the sensor

The basic construction of the sensor comprises three parts: a soft spring, a stiff spring, and two grips to hold a self-assembled tissue construct. Figure 1 (A and B) presents schematic diagrams and working mechanisms of the sensors. The soft spring (blue spring; Fig. 1, A and B) is the force-sensing component, and the stiff spring (brown spring; Fig. 1, A and B) helps to hold the tissue in plane. Their stiffness is denoted by K_s and K_r, respectively. Each of the springs is connected to a grip so that any force on the grips can be transferred to the springs. The tissue is formed by dispensing a droplet of liquid cell-ECM (rat tail collagen I) mixture with low cell density on the grips (Fig. 1A and movie S1). Cell density of the cell-ECM suspension is so chosen that the droplet contains only a single cell or a discrete number of cells. The liquid cell-ECM mixture fills the gaps of the grid and forms a capillary bridge between them (movie S1). Collagen polymerizes within about 10 min and results in a tissue with a single cell (Fig. 1A) or multiple cells (Fig. 1B). The initial length of the tissue is denoted by L_0. As the cell(s) starts to activate, it engages with the collagen fibers, elongates, and generates contractile force, F. The force is transferred to the grips, and the soft spring extends by d_c, giving cell force, $F = K_s * d_c$. As the stiffness K_r is very high, extension of the rigid spring is negligible ($F/K_r \approx 0$). Hence, the length of the contracted tissue is $L_c = L_0 - d_c$.

Figure 1B illustrates the method of measuring the stiffness of the tissue. To measure the compressive stiffness of the cell-ECM tissue, the stiff spring is pushed toward the tissue so that it is compressed to a length of L'_c from its initial resting length of L'_0 before actuation. Let d'_c be the corresponding deformation of the spring from its rest configuration. Here, the tissue deformation is $\Delta L'_c = |L'_c - L'_0|$, and the axial compression force on the tissue (and the springs) is $F'_c = K_s * d'_c$. Hence, the compressive stiffness of the tissue can be determined as $K_c = dF'_c/d(\Delta L'_c)$ at $\Delta L'_c$. For measuring tensile stiffness of the tissue, the stiff spring is pulled outward so that the tissue and the springs are all in tension, and the tensile stiffness of the tissue is determined as $K_t = dF'_t/d(\Delta L'_t)$ at $\Delta L'_t = L'_t - L'_0$, where F_t is the axial tension and deformation is $\Delta L'_t$.

Figure 1C shows a simple design of the sensor. The thin beams represent the soft spring, while the thick beams form the rigid spring. The beams are anchored at one end that allows no rotation or translation. The other ends are rigidly attached to the grid frame that restricts rotation but allows horizontal translation. Figure 1D shows the deformed beams (spring) when cell(s) applies a force dipole within the tissue. Stiffness of a spring with n beams is $K_s = 12nEI/L^3$, where E, I, and L are the modulus of elasticity of PDMS (1.7 MPa), the moment of inertia ($I = hb^3/12$,with b and h being the width and depth of the beams), and the length of the beams, respectively. Hence, the stiffness and resolution of the sensor can be controlled by varying the width and length of the beams. For example, K_s = 4.6 nN/μm, for one of our fabricated sensors with four beams, each 30 μm wide, 200 μm deep, and 2000 μm long. However, it is possible to fabricate thinner beams for sensors with higher sensitivity. An enlarged image of the tissue and gauges for measuring spring deformation is presented in Fig. 1E. A perspective view of the setup is also given in Fig. 1F. Note that the gauges are placed away from the center of tissue location so that the design allows measurement of force as a function of time without directly illuminating the cell(s). This eliminates the possibility of light-induced response of the cells (*44*, *45*).

Figure 1G presents a simplified cartoon of force generation by cells and transmission mechanisms to the sensing springs. First, the cell establishes focal adhesion with the ECM and then starts to contract. As the cell pulls onto the collagen fibers, they get stretched and transmit the tension to the grips and, thus, to the sensing springs. During this process, some cross-links between collagen fibers break, while some new ones form. With time, the cell increases contractility, which results in higher force output. Again, when the cell retracts from focal adhesions during migration or altering polarities, its traction with the ECM decreases, and the force output also decreases.

Setup and operation

We used standard photolithography and deep reactive ion etching (DRIE) techniques to prepare molds from silicon wafers for the PDMS sensors (details in Materials and Methods). Figure 2 (A and B) shows the fabrication process in a setup petri dish.

To have a resolution capable of sensing single-cell forces, the sensor springs (beams) must be very soft for high sensitivity. The softness makes the sensor vulnerable to failure because of meniscus forces (surface tension) that appear during its inundation from air to the media. Meniscus forces cause large deformation, buckling and twisting of the sensor beams, and stiction between them. To overcome this problem, we established an innovative protocol that uses a sacrificial material to protect and anchor the soft beams from exposure to meniscus forces until the ECM is cured and immersed under culture media. We found gelatin to be the ideal sacrificial material for restraining the springs since it is biocompatible and solid at room temperature and fully dissolves in water at temperatures over 37°C (*46*). Figure 2B shows a step-by-step process for the experimental setup. First, an elevated platform is prepared by sticking a glass block to the bottom of a petri dish. Then, a layer of gelatin is placed so that the sensor springs do not stick to the bottom. The PDMS sensor is then attached to the platform using liquid PDMS as glue (Fig. 2B). The connector between the soft spring and its support beam is then severed. Another layer of gelatin is poured on the sensor, only leaving the tissue formation site and the grips unfilled.

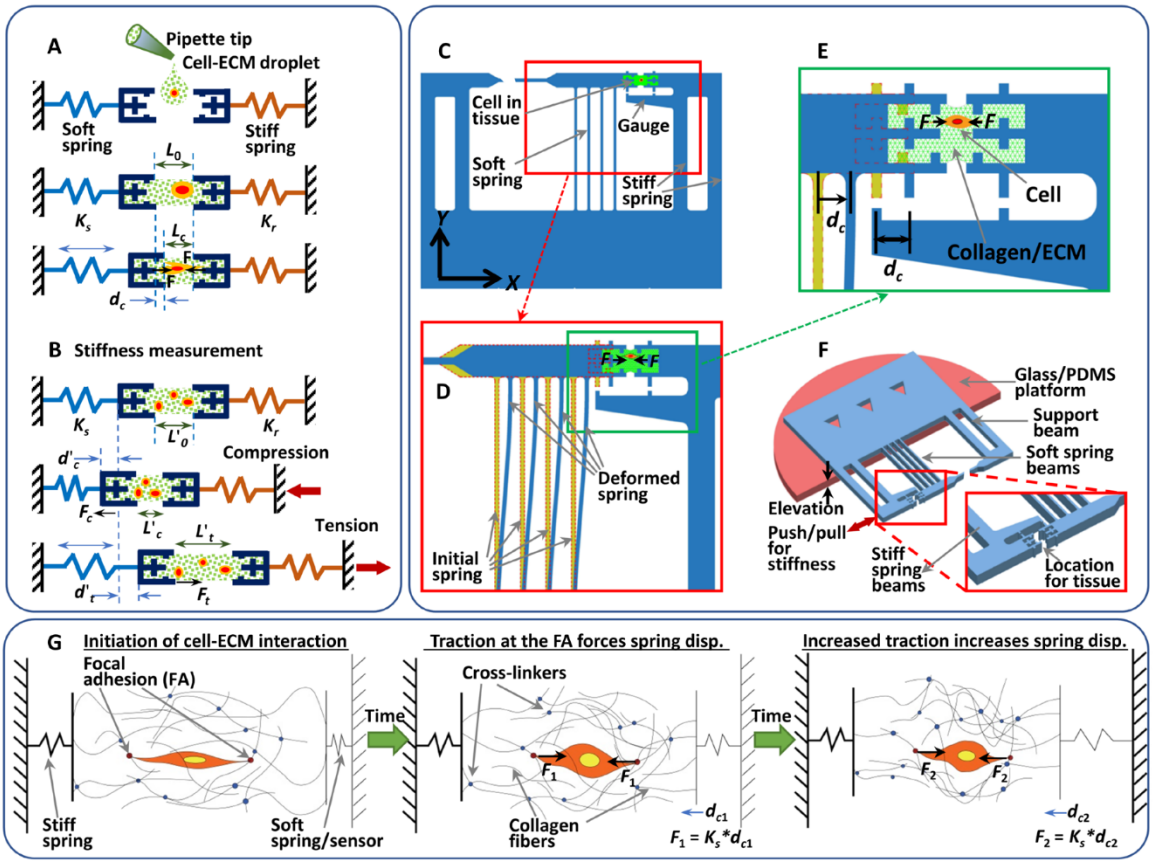

Fig. 1. Schematic representation of the concept, design, and functional mechanics of the sensor. (**A**) Simplified model for measurement of cell traction force in 3D matrices. A tissue is formed by dropping cell-ECM mixture between grips connected to springs of known constants. Traction generated by cells in the tissue transfers to the springs and deforms the sensing spring (blue). Cell force is quantified as the product of spring constant and deformation (K_s*d_c). (**B**) Technique for measurement of stiffness of the tissue on the sensor. Compressive stiffness can be measured by pushing the stiff spring inside, while tensile stiffness can be measured by pulling the tissue. During the stain application, we continuously monitor the gauges that read the force and strain. (**C**) Design of the sensor. The thin and wide beams represent the soft and stiff springs, respectively. (**D**) Deformed shape of the beam springs due to cell traction. (**E**) Enlarged figure of the tissue and the gauges. (**F**) Experimental setup. (**G**) Cell activity within 3D ECM and how cell forces transfer through the matrix fibers to the springs.

A droplet of liquid cell-ECM mixture is dispensed between the grips, which fills up the space and wets the grips due to capillarity. We then apply a vacuum (~50 kPa, 20 s) to remove any air bubble. The ECM is then polymerized at room temperature, after which the setup is immersed in cell culture media and incubated at 37.5°C for about 30 min. During this period, gelatin melts and dissolves in the media, which is later washed out and replaced with fresh media. Thus, the sensor and the tissue bridge never get exposed to air-water meniscus forces. The setup is placed in an environment-controlled chamber with a microscope for long-term imaging of the gauge and the tissue. The gauge gives force readout with time, and the tissue images allow monitoring of cellular activities.

Finite element analysis

To investigate how cell position and orientation may affect the force readout from the sensor, we carried out detailed finite element analysis (FEA) of the sensor-tissue system. PDMS was simulated as a linear elastic material with modulus of elasticity, E = 1.7 MPa (*47*). Collagen was modeled as a bilinear elastic material with compressive modulus significantly lower than tensile modulus ($E_{tension}$ = 1000 Pa and $E_{compression}$ = 0 0.001 Pa) (*33*, *48*, *49*). Figure 3 (A to D) shows the model and results from the FEA. Three cases were studied where the cell force dipole (two point forces 50 μm apart) was (i) aligned, (ii) at 45°, and (iii) perpendicular to the sensing spring axis (Fig. 3D). The dipole was applied at the center of the tissue, and the deformed configuration for the horizontal orientation is shown in Fig. 3 (B and C). We also varied the dipole force magnitude from 0 to 50 nN. Displacement readout, d_c ($F = K_s * d_c$), from the springs shows a linear correlation with applied force (Fig. 3D). For the cell aligned with the spring axis, the sensor reads the total force. With the cell orientation deviating from the spring axis, the sensor reads the total force component along the spring axis.

We also found that the spring deformation, d_c, is almost independent of the location of a horizontal force dipole (Fig. 3E). For any position of the applied dipole, readout is within 5% of the applied force. We also found that cells inside the grips do not interfere with the force readout by cells within the tissue (Fig. 3F). In all such intra-grip dipole cases, the spring displacement is negligible, ascertaining that the sensor reports data for only those cells that are positioned between the two grips.

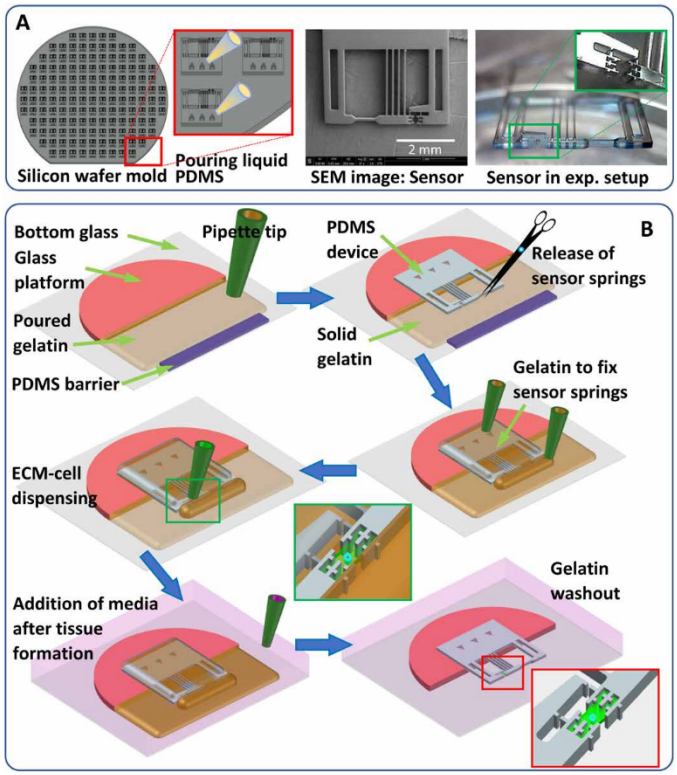

Fig. 2. Fabrication of the sensors and preparation of experimental setup. (**A**) A silicon wafer mold is prepared using photolithography and microfabrication. The sensors are cast from the molds by pouring liquid PDMS and curing at 60°C overnight. Scanning electron microscopy (SEM) image displays a complete sensor. Photo of the setup shows a sensor ready for experiments. The inset presents a zoomed-in image of the tissue grips. Photo credit: Bashar Emon, University of Illinois at Urbana-Champaign. (**B**) Operational scheme to overcome surface energy–related challenges for the sensor. Step 1: Sticking a glass platform and a PDMS barrier to the bottom glass of a petri dish using liquid PDMS and then preparing a gelatin substrate. Step 2: Placing the sensor on the solid gelatin substrate, sticking the sensor base to the glass platform, and then cutting the connector. Step 3: Pouring liquid gelatin on the sensor beams and other components, except near the grips. If needed, solid gelatin barriers can be created to secure the grips beforehand. Step 4: Upon gelation of gelatin at room temperature, dispensing of cell-collagen mixture onto the grips to form the tissue. Capillary tension should help collagen fill out gaps in the grips. Step 5: After forming the tissue by polymerization at room temperature, submerging the whole setup in cell culture media and incubation at 37°C for 30 min. Step 6: Carefully performing washout three times to remove residual gelatin.

Force and stiffness dynamics

Cell traction and ECM remodeling are continuous interdependent processes. We have tested the sensor for time-lapse force imaging of single and multiple cells for durations of at least 16 hours. We imaged every 5 min for temporal variations in force. However, imaging frequency can be increased without any additional adjustments for experiments that focus on faster response from the cells. Force resolution of the sensor depends on the spring stiffness and the image analysis protocol. Our current setup has an image resolution of 167 nm per pixel, which yields a displacement resolution of approximately 17 nm when analyzed with sub-pixel registration in ImageJ (*50*, *51*). This results in a force resolution of approximately 0.08 nN (K_s = 4.6 nN/μm). However, noise analysis with control specimens reveals that the system has a resolution of ~1 nN (fig. S4).

For the current study, we chose NIH 3T3 mouse fibroblasts as a conventional cell line and CAF05 (human colorectal cancer–associated fibroblasts) as representative cells for human cancer-related experiments. Figure 4A (movie S2) and Fig. 4B (movie S3) show cell forces by a single 3T3 fibroblast and a single CAF05, respectively, resolved in the axial direction. Representative phase-contrast images of the tissue (cells) are also shown at different time points. We observed that each of these cells initially increase their forces gradually, with small fluctuations. During this period, the cells generally probe its microenvironment by protruding small filopodia and pulling the fibers. When the cells elongate and polarize, the magnitude of force increases and so do the fluctuations. For example, the CAF started to elongate at around the 12th to 15th hour, and the force versus time curve also shows spikes in force at the same time. The 3T3 cell exhibits such peaks and drops in forces after the 10th hour. These observations are consistent with the fact that cells increase and relax traction periodically while migrating (*21*, *52*). The maximum force by the 3T3 cells was ~20 nN, while the CAFs generated a maximum of ~50-nN force. However, fibroblasts on 2D substrates with stiffness comparable to collagen (~300 Pa) can produce force of ~100 nN (fig. S1B) (*53*). With higher stiffness, the force can considerably increase to a few micronewtons (fig. S1A). Thus, cell forces measured by 2D TFM can be significantly higher than cell forces in 3D ECM or in vivo. Time-resolved cell forces for single CAFs presented in fig. S1 highlight these interesting distinctions between 2D and 3D culture conditions.

Moreover, the phase-contrast images show, for both cases, that when the cells are more elongated, i.e., polarized, the magnitude of their forces is much higher compared to the forces when they were not polarized. This finding is consistent with previous studies (*33*, *54*) that reported that traction forces increase with distance of focal adhesions from the cell center. Possible mechanism for this phenomenon involves protrusion-retraction and actin flow at the cell edge while migrating and polarizing (*54*). Insets show finer variations of force. For periods of time, the cells maintain force homeostasis, which is evident when the force readout is constant. Another interesting observation is that duration for increasing force is considerably shorter than that for relaxation. This means that the rate of contraction is considerably faster than the rate of relaxation. These findings provide unique insights into cellular force dynamics in 3D ECM.

We also constructed tissue with a small number of cells to observe the collective contractility behavior of fibroblasts. However, the number of cells was kept small enough so that individual cell activities can be tracked. Force evolution with multiple cells demonstrates higher magnitudes, but the magnitude does not increase linearly with cell number (Fig. 5, A and B). Phase-contrast images and corresponding resultant force by a collection of 3T3 fibroblasts are presented in Fig. 5A (movie S4). Images of the tissue show that cells elongate and migrate in the 3D ECM. In addition, similar to the single-cell experiments, the curve displays short pulses of force relaxation. However, tissues with multiple cells do not demonstrate a faster contraction rate than relaxation, unlike single cells. A possible reason is that the sensor detects the summation of force contributions from each cell, and these cells are often not synchronized. Thus, these cells' random orientation and out-of-phase activities produce a resultant force readout that has similar rates of contraction and relaxation, unlike that of single cells. Data for four active CAFs are shown in Fig. 5B (movie S5). Similar to single cells, this curve also exhibits periods of steady state, with occasional increase

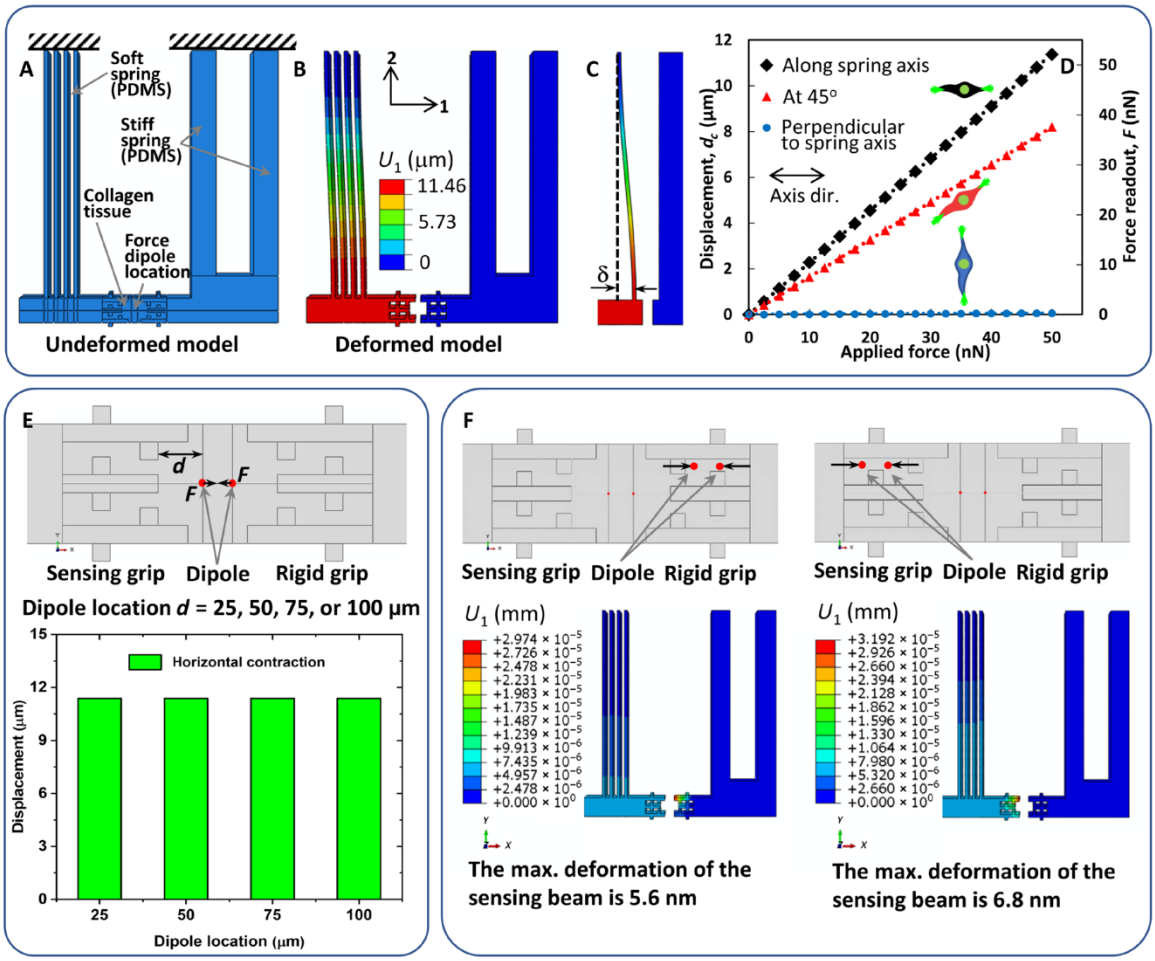

Fig. 3. FEA verifies that the sensor can reliably detect cell forces. (**A** to **D**) The undeformed and deformed models show the strains on the beam springs. The graphs show the relation between cell alignment, force input, and readout from the sensor. Evidently, the sensor precisely detects the force component along the spring axis. (**E**) Position of the force dipole (or cell force) within the tissue does not affect the sensor's force detection. (**F**) Force applied inside the grips of the tissue does not transfer to the sensing spring. Hence, it can be claimed that the force output from the sensor is the result of traction by only the cells residing between the grips.

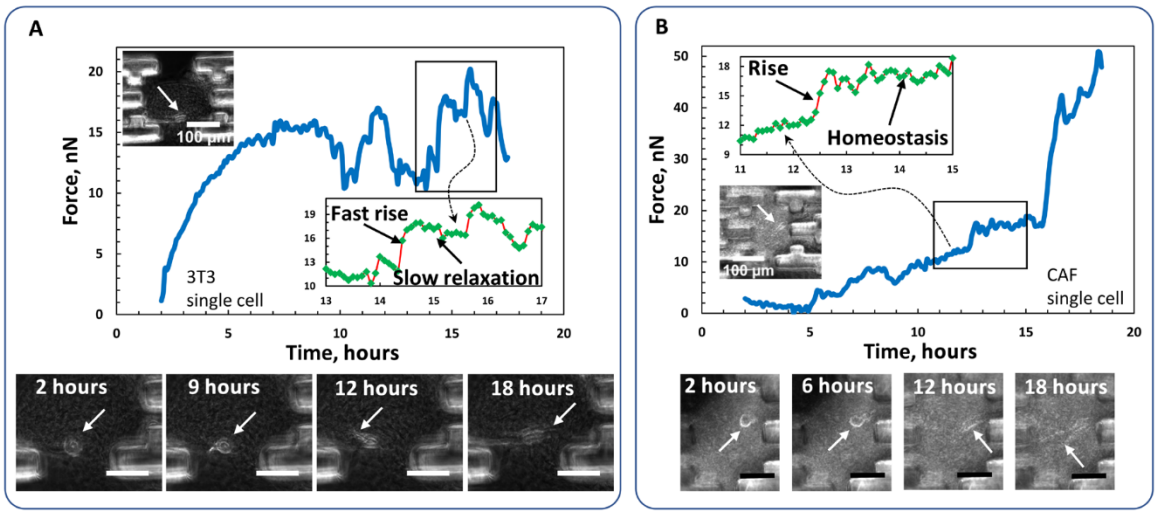

Fig. 4. The sensor is capable of detecting single-cell forces and small fluctuations in 3D collagen. Traction force evolution of single (**A**) 3T3 and (**B**) CAF05 fibroblasts. The insets enlarge part of the curves to highlight each data collection point and local dynamics of contraction and relaxation. Phase-contrast images show the cells in the tissue that are generating the force curves. White arrows indicate the location of the cells in the tissues. Scale bars, 100 μm.

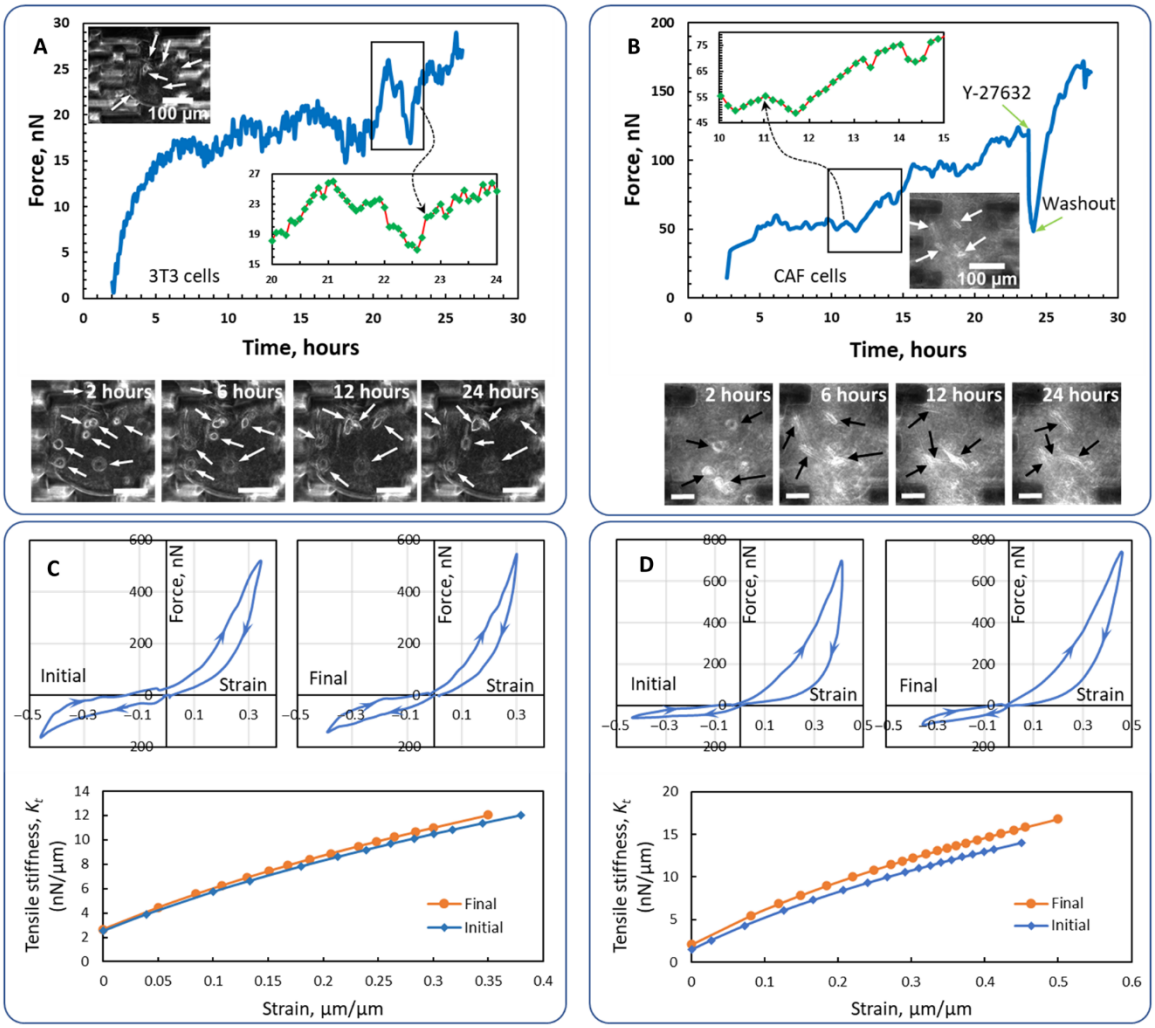

Fig. 5. The sensor can measure multiple cell forces and change in tissue stiffness with time. Traction force evolution of multiple (**A**) 3T3 and (**B**) CAF05 fibroblasts. The insets enlarge parts of the curves to highlight each data collection point and local dynamics of contraction and relaxation. Phase-contrast images show the cells in the tissue that are generating the force curves. Arrows indicate the locations of the cells in the tissues. Scale bars, 100 μm. Force versus strain curves and corresponding tensile stiffness graphs of the tissues with (**C**) 3T3 and (**D**) CAF05 fibroblasts. The compression-tension tests were performed at the start of the experiment when the cells were still not activated and after about 24 hours. The curves show that the cells increased the stiffness of the tissues very slightly in this period.

in force. To confirm that the output force is generated by the cells, we applied Y-27632 that inhibits Rho-associated kinase signaling pathways to relax cell traction. As expected, within 20 min, the drug reduced the force by about 60%. After washout at this point, the cells immediately started to contract and reestablished predrug level of force in about 1 hour. The cells continued to increase force for the following 2 hours. This indicates that the forces detected by the sensors are generated by the cells within the 3D collagen tissue. To provide a glimpse into sample-to-sample variations in cell/tissue forces, we present data from several specimens for the same type of tissue (of same cell type) in fig. S2.

Moreover, we assessed mechanical changes of collagen due to remodeling by the CAFs and 3T3 fibroblasts, in terms of stiffness of the tissue. To this end, the tissue stiffness was measured at the 2nd hour (initial) and 28th hour (final) of tissue formation. Movie S6 shows the process of applying strains on the tissue for stiffness measurement. Force versus strain curves for both compression and tension with 3T3s and CAFs are shown in Fig. 5 (C and D, respectively). During the loading-unloading cycle, we performed compression first and then tension. Both compression and tension curves show nonlinear relations. It is also evident that the tissues have higher stiffness in tension compared to that in compression. This indicates that the sensor is capable of reliable mechanical testing of micrometer-scale soft specimens since it can capture behavior of polymeric scaffolds such as collagen (*55*–*57*). The tension-loading portions of the curves were fitted to the Mooney-Rivlin model for hyperelastic materials. The tangential tensile stiffness (K_t) was derived from the fitting model, and variations of K_t with increasing strains are also presented in Fig. 5 (C and D) (details in Materials and Methods and the Supplementary Materials). Both CAFs and 3T3 cells increased the stiffness of the tissues very slightly in about 24 hours. We understand that the tissue requires more cells or time to make significant remodeling, but the sensor can detect subtle changes in the stiffness.

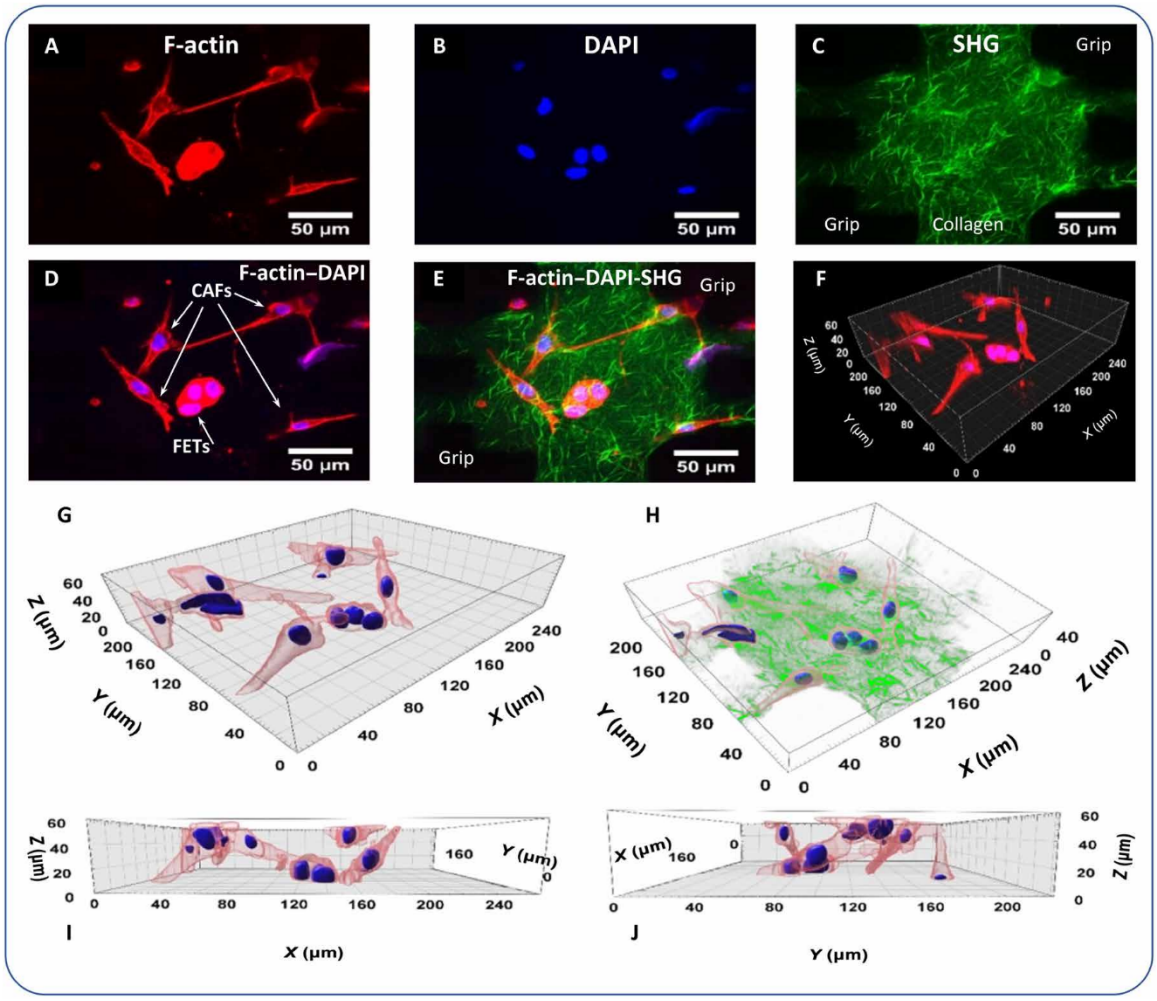

Fig. 6. 3D tumor model on the sensor with cancer cell and CAF coculture. (**A**) Maximum intensity projection of F-actin labeled with phalloidin conjugated with Alexa Fluor 647. (**B**) Maximum intensity projection of cell nuclei labeled with 4′,6-diamidino-2-phenylindole (DAPI). (**C**) SHG image of collagen fibers. (**D**) Overlay image of the F-actin and nuclei of the cells. (**E**) Overlay image of the F-actin, collagen fibers, and nuclei of the cells. (**F**) 3D reconstruction of confocal z-stacks of F-actin and nuclei of the cells. (**G**) 3D surface rendering of confocal z-stacks of F-actin and nuclei of the cells. (**H**) Overlay image of collagen fibers and 3D surface rendered image of F-actin and cell nuclei. (**I**) *XZ* and (**J**) *YZ* plane of 3D rendered surface from (G).

Tissue with cancer cells

To demonstrate potential application of the sensor to study in vitro tissues that mimic tumor microenvironment (TME), we created lung cancer and colorectal cancer (CRC) models on the sensors with A549 (human lung epithelial carcinoma) and human CRC cell lines. Figure 6 demonstrates the sensor's capability to host a 3D in vitro tissue model where cancer and stromal cells reside in close proximity of each other. The confocal images show that the model consists of one FET CRC cluster with three cells, five CAF05 stromal fibroblasts, and collagen as ECM scaffold. Confocal z-stack images of labeled F-actin and nuclei (Fig. 6, A and B) of the cells were used to reconstruct the 3D structure of the cells, while the two-photon second harmonic generation (SHG) images (Fig. 6C) show the collagen organization around the cells. 3D reconstruction of the tumor tissue (Fig. 6, D to J, and movie S7) validates that the model offers a 3D culture condition necessary for simulating TME.

For force dynamics evaluation, we constructed three different tissues with (i) A549 cells (Fig. 7A and movie S8), (ii) FET (human colorectal carcinoma) cells alone (Fig. 7, B and D, and movie S9), and (iii) FET and CAF05 (human colorectal CAFs) cells together (Fig. 7, C and E, and movie S10). Most of the A549 lung cancer cells are initially singular (Fig. 7A, 2 hours) like the fibroblasts, but with time, they coalesce into a number of small clusters (Fig. 7A, 18 hours). However, FET cancer cells are different from the fibroblasts in terms of cell-cell adhesion and migration. Initially, FET cells form small clusters (Fig. 7B), whereas fibroblasts remain as individual cells (Fig. 5, A and B). With time, these small clusters of FET cells combine into larger clusters, forming cancer spheroids that are single compact bodies that contain all the cells in the microtissue. The spheroids inside 3D collagen are dynamic; they continuously evolve into different shapes and sizes and also maintain traction with the ECM. However, unlike the FET cells, A549 cells did not form large spheroids, even after 30 hours.

Evolution of force within a 3D collagen matrix by A549 and FET cancer cells is shown in Fig. 7 (A and B). The force history of A549 cells appears to be similar to those of fibroblasts (Fig. 5A). The FET

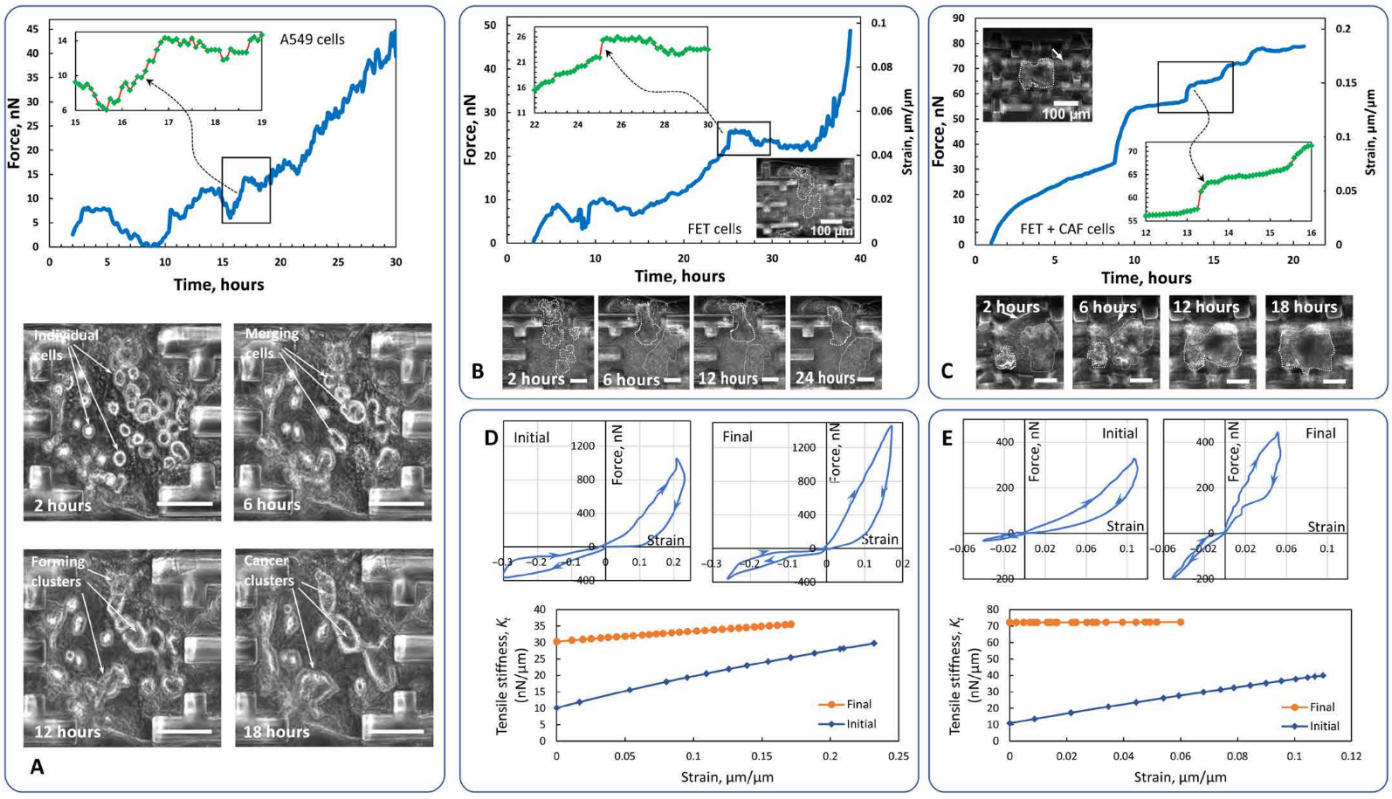

Fig. 7. Cell traction and matrix stiffening in cancer. Traction force evolution of a cluster of (**A**) A549 lung cancer cells (**B**) FET CRC cells and (**C**) FET and CAF05 fibroblast coculture tissue. The insets enlarge parts of the curves to highlight each data collection point and local dynamics of contraction and relaxation. Phase-contrast images show that the cells merge into clusters and spheroids in the tissue. White dotted lines indicate cell cluster boundaries, and the arrows indicate the location of a CAF cell in the tissues. Scale bars, 100 μm. Force versus strain curves and corresponding tensile stiffness graphs of the tissues for (**D**) FET only and (**E**) FET and CAF05 coculture. The compression-tension tests were performed at the start of the experiment and after about 24 hours. Both curves show that the cells significantly increased the stiffness of the tissues, which indicate substantial remodeling.

force history (Fig. 7B), however, exhibits a distinct feature, i.e., there are very few drops in force, unlike those for the A549s (Fig. 7A) and fibroblasts (Fig. 5, A and B). One potential reason is that the spheroids do not migrate as much as the A549s and fibroblasts (movie S9). The dynamic force that these spheroids generate results in significant stiffening of the surrounding ECM. Figure 7D shows that the cancer spheroids significantly increased (minimum, 40%; maximum, 200%) the stiffness K_t of the tissue in about 40 hours.

To mimic a 3D TME, we created a tumor tissue on the sensor with FETs and CAFs in collagen. Coculture of cancer and stromal cells facilitates various signaling and cross-talk between them (*7*, *58*, *59*). For this specimen, the small FET clusters agglomerate and form a larger spheroid, but the CAFs remain as isolated cells and move around the spheroid (movie S10). Overall, the coculture specimen showed a stronger force output and ECM stiffness change. The force curve in Fig. 7C shows that the tissue slowly increases force without relaxation at any point and occasionally generates forces at high rates. In addition, this specimen underwent a greater remodeling, as indicated by almost threefold increase in K_t (minimum, 133%; maximum, 600%; Fig. 7E). Thus, these experiments demonstrate that the sensor can be a suitable tool for biophysical investigation of cancer cells, stromal cells, and the TME. For instance, we can examine the effect of stiffness of TME on cross-talk between cancer and stromal cells or metastatic migration of invasive cells. It is possible to create ex vivo tumor tissues on the sensors using primary cells derived from biopsy samples and using traction force/stiffness for personalized drug screening.

Limitations and future directions

Cell contractility and cell adhesion to 3D matrices induce a 3D traction field within the fibrous network. As mentioned earlier, the current uniaxial sensor bypasses determination of the stress fields and is designed to measure the resultant force projected/resolved along the spring axis. As a result, force components generated by the cells along other two normal directions cannot be detected by the sensor in its current form; hence, the total cell/tissue force can be underestimated (Fig. 3D). However, with minor modifications to the design, one can easily add another orthogonal sensing spring in the *XY* plane (Fig. 1). The addition of a spring in the *Z* axis poses considerable fabrication and operational challenges; nevertheless, we believe that it is possible. Such devices with three orthogonal sensors can measure forces resolved in 3D and thus provide a remedy to current limitations. Hence, we suggest careful interpretation of force results from the current sensor, especially with regard to cellular arrangement, alignment, and heterogeneity within the tissue. Similarly, the sensor's uniaxial tension/compression testing provides 1D stiffness measurement. A second sensing spring may allow biaxial stiffness measurement, which may lead to interesting findings about the nature

of mechanical changes (e.g., isotropic or anisotropic) due to remodeling activities of the cells. Furthermore, the sensor can apply mechanical stimulation to cells by stretching and contracting the tissue, which is relevant in many biophysical processes.

Another limitation of the current data acquisition system is the phase-contrast microscopy since this technique can only provide projected 2D information. While phase-contrast imaging is sufficient for observation of the gauges, it certainly is not adequate to make 3D spatial correlations. This drawback can be overcome with tomographic imaging (e.g., confocal and multiphoton) that can provide a comprehensive visual into the real cellular and scaffold orientation and microstructure. Moreover, complementing the sensor with matrix deformation measurement techniques may uncover exciting avenues to explore. For example, we can easily embed fiducial beads within the matrices and use kinematics-based methods to reconstruct 3D deformation field that correlates with the force readout. Such analysis can offer new insights into cell traction and relevant biological processes.

For the data presented in this paper, we only considered collagen scaffolds for preparation of self-assembled microtissues on the sensors. However, other natural and synthetic matrices, such as Matrigel and poly(ethylene glycol) diacrylate (PEGDA), can also be used for constructing the tissues. We have already shown that samples can be prepared with neurons and muscle cells in Matrigel- or collagen-Matrigel–based matrices. The only limitation is that the polymerization temperature of the matrix needs to be below 37°C. This is to ensure that gelatin anchors can retain shape during the process of tissue formation since gelatin melts at 37°C. Another potential application of the sensor platform can be with architected biomatrices, e.g., 3D printed, electrospun scaffolds to precisely control fiber arrangement and orientations. This technique can enable measurement of resolved total force by aligning cell(s) in the sensing directions.

CONCLUSION

We developed a high-resolution sensor that allows self-assembly and culture of 3D tissue models and described the basic principles of the design and analysis and its methods of operation. The sensor can report single- and multiple-cell forces in 3D ECM over a long period of time with a resolution of 1 nN and quantify the change of stiffness of the tissue remodeled by the cells. Feasibility of the sensor was tested by forming tissues with a single 3T3 fibroblasts and CAF05 cells (human colon cancer–associated fibroblasts) and with multiple cells (3T3, CAF05, human colon cancer cell FET, and human lung cancer cell A549). Single 3T3 cells produced a maximum of ~20 nN, while single CAFs produced up to ~50 nN. Their corresponding forces on 2D substrates with similar stiffness approach ~100 nN. Multiple cells exhibit higher overall force collectively, although the magnitude does not scale linearly with the number of cells. In terms of remodeling, 3T3 fibroblasts or CAFs (<10 cells) did not induce any significant change in stiffness of the tissues. On the other hand, FET and A549 cancer cells form clusters, generate large force, remodel the matrix, and increase the stiffness by about 200% (maximum) in 24 hours. FET and CAF05 coculture changes stiffness with a maximum of 600%. In summary, the microsensor allows measurement of single- and multiple-cell forces in 3D matrices and quantification of tissue stiffness change due to ECM remodeling. An array of such sensors can be applied to form tumor environments from patients' cell for drug screening and prognosis.

MATERIALS AND METHODS

Cell culture

Human primary colorectal tumor CAFs, CAF05 (Neuromics, Edina, MN, USA), were maintained in VitroPlus III Low Serum, Complete medium (Neuromics, Edina, MN, USA). NIH 3T3 cells, obtained from the American Type Culture Collection (ATCC) (Manassas, VA, USA), were cultured in fibroblast media prepared with Dulbecco's modified Eagle's medium (DMEM; Corning), 10% fetal bovine serum (FBS; Gibco), and 1% penicillin-streptomycin (Lonza). FET human colorectal carcinoma cells were a gift from the laboratory of B. Jung, Department of Medicine, University of Illinois at Chicago and were maintained in 89% DMEM/F12 50:50 (Gibco), 10% FBS (Gibco), and 1% penicillin-streptomycin (Lonza). A549 lung cancer cells were collected from F. Kosari, Mayo Clinic, Rochester, MN. These cells were cultured in F-12K medium (Kaighn's modification of Ham's F-12 medium; ATCC, Manassas, VA) supplemented with 10% FBS (Gibco). Cells were grown at 37°C in a humidified incubator with 5% CO_2.

Fabrication and assembly of PDMS sensors

The sensors were cast from microfabricated silicon molds. Standard 500-μm silicon wafers (University Wafer, Boston, MA, USA) were patterned by photolithography and etched to a nominal depth of 200 μm using the DRIE process (STS Pegasus ICP). Next, the etched wafers were coated with polytetrafluoroethylene to facilitate removal of PDMS from the mold. PDMS (SYLGARD 184) base and cross-linker were mixed at 10:1 ratio by weight, pipetted into the molds, and allowed to fill all the features and trenches by capillary mircomolding (*60*). The specimens were cured at 60°C for 12 hours and lifted off the silicon molds. For assembling the setup, a rectangular glass piece (#2 cover glass, Corning) was glued to the bottom glass of a glass-bottom petri dish (diameter, 60 mm; Corning) using uncured PDMS. The glass piece served as the elevated platform. The sensors were also fixed to the glass platform using uncured PDMS. We arranged 10 to 15 single sensors in one 60-mm petri dish. Scanning electron microscopy (SEM) imaging of the sensor was performed with FEI Quanta FEG 450 ESEM.

Tissue formation

For preparing all tissue precursor solutions, an ECM solution was prepared on ice by first neutralizing rat tail collagen I (Corning) with 1 M sodium hydroxide, 10× phosphate-buffered saline (PBS), and deionized water. We followed Corning recommended protocol (*61*) to prepare a final collagen solution of 2 mg/ml with pH 7.2 from a high-concentration stock solution of 8.9 mg/ml in 0.02 N acetic acid. For a single cell in the tissue, cells were suspended in the ECM solution at a density of 150×10^3 cells/ml. Cell density was increased linearly on the basis of the desired number of cells in the final tissue construct. Cell-ECM mixture was then pipetted onto the grips of the sensors and was allowed to fill the channels. A syringe pump (NE-1000; New Era, Farmingdale, NY) was used to control pumping of the liquid mixture through a flexible tube to a fine needle with precise volume and flow rate. The needle was fixed to a 3D automated stage equipped with piezo-actuators with fine steps (few nanometers) to precisely dispense cell-ECM mixture onto the space

between the two grids (movie S1). All the components are kept at 0°C before dispensing to avoid early polymerization of ECM.

In general, capillary tension is enough to draw the mixture in and drive the air pockets out; however, removal of persistent bubbles can be aided by applying low-pressure for about 20 s in a vacuum desiccator. Until this point, the procedures were carried out on ice to delay the onset of polymerization. After removing any remaining air bubbles, the cell-ECM mixture was allowed to polymerize at room temperature for 10 to 15 min; then, the sensors with assembled tissues were inundated in culture media and placed in the incubator.

Immunohistochemistry and imaging

The setup was placed, for the duration of the experiment, in an environment-controlled chamber enclosing an inverted optical microscope (Olympus IX81, 40× objective, Olympus America Inc., Center Valley, PA) mounted on a vibration isolation table (Newport Corporation, Irvine, CA). The chamber maintains cell culture conditions at 37°C temperature, 5% CO_2, and 70% humidity. Moreover, a motorized stage (Prior Scientific Inc., Rockland, MA) allowed automatic imaging of multiple specimens at preset locations at multiple time points. Images of both the tissues and the gauges were acquired in phase contrast or bright-field mode with a Neo sCMOS camera (active pixels, 1392 × 1040; resolution of 167 nm per pixel) (Andor Technology, Belfast, Northern Ireland). For calculating spring displacements, images of the sensor gauges were analyzed using template matching plugin in ImageJ with sub-pixel resolution, and the resolution was approximately 17 nm.

For confocal imaging, the samples were fixed with 4% paraformaldehyde in PBS for 1 hour. Subsequently, 0.2% Triton X-100 in PBS was used to permeabilize the samples and 2.5% bovine serum albumin with 2% normal goat serum in PBS was used as a blocking solution. Samples were then incubated overnight in phalloidin conjugated with Alexa Fluor 647 (1:40; Invitrogen, Carlsbad, CA, USA) at 4°C. Afterward, the samples were washed with PBS three times and then incubated in 4′,6-diamidino-2-phenylindole (1:1000; Invitrogen, Carlsbad, CA, USA) for 10 min and washed with PBS again. The image acquisition was done with a confocal microscope, LSM710, using an EC Plan-Neofluar 20×/0.5 numerical aperture objective lens (Carl Zeiss AG, Oberkochen, Germany). SHG images are acquired subsequently using the same LSM710 two-photon excitation microscope and 20× objective. Maximum intensity projection of the acquired confocal z-stacks was constructed using the ImageJ [U.S. National Institutes of Health, Bethesda, MD, USA] software, and Imaris (version 9.6.0; Bitplane AG, Zurich, Switzerland) was used for the 3D surface rendering.

Finite element analysis

3D FEA was performed using commercial software Abaqus to investigate the beam deformation of the force sensor under the cell contraction. Eight-node brick solid elements (C3D8R) were used to discretize the geometry of force sensor and ECM, and refined meshes were adopted to ensure the accuracy. The force sensor has four parallel aligned beams with 30-μm gaps in between, and each of the beams has the length of 2000 μm, width of 30 μm, and depth of 200 μm. The cell contraction was simulated by applying 50-nN dipole forces with 50-μm distance. Linear elastic model was used to demonstrate the material behavior of PDMS force sensor and ECM. The elastic moduli (E) and Poisson's ratios (υ) used are $E = 1.7$ MPa and $\upsilon = 0.48$ for the PDMS sensor. For ECM, the tensile elastic modulus and compressive modulus are 1 kPa and 0.001 Pa, respectively, and the Poisson's ratio is 0.48.

SUPPLEMENTARY MATERIALS

Supplementary material for this article is available at http://advances.sciencemag.org/cgi/content/full/7/15/eabf2629/DC1

View/request a protocol for this paper from *Bio-protocol*.

REFERENCES AND NOTES

1. M. S. Sakar, J. Eyckmans, R. Pieters, D. Eberli, B. J. Nelson, C. S. Chen, Cellular forces and matrix assembly coordinate fibrous tissue repair. *Nat. Commun.* **7**, 11036 (2016).
2. B. Li, J. H.-C. Wang, Fibroblasts and myofibroblasts in wound healing: Force generation and measurement. *J. Tissue Viability* **20**, 108–120 (2011).
3. A. M. Handorf, Y. Zhou, M. A. Halanski, W.-J. Li, Tissue stiffness dictates development, homeostasis, and disease progression. *Organogenesis* **11**, 1–15 (2015).
4. M. R. Zanotelli, C. A. Reinhart-King, in *Advances in Experimental Medicine and Biology* (Springer, 2018), vol. 1092, pp. 91–112.
5. W. J. Hadden, J. L. Young, A. W. Holle, M. L. McFetridge, D. Y. Kim, P. Wijesinghe, H. Taylor-Weiner, J. H. Wen, A. R. Lee, K. Bieback, B. N. Vo, D. D. Sampson, B. F. Kennedy, J. P. Spatz, A. J. Engler, Y. S. Cho, Stem cell migration and mechanotransduction on linear stiffness gradient hydrogels. *Proc. Natl. Acad. Sci. U.S.A.* **114**, 5647–5652 (2017).
6. S. Li, N. F. Huang, S. Hsu, Mechanotransduction in endothelial cell migration. *J. Cell. Biochem.* **96**, 1110–1126 (2005).
7. B. Emon, J. Bauer, Y. Jain, B. Jung, T. Saif, Biophysics of tumor microenvironment and cancer metastasis—A mini review. *Comput. Struct. Biotechnol. J.* **16**, 279–287 (2018).
8. F. Broders-Bondon, T. H. N. Ho-Bouldoires, M. E. Fernandez-Sanchez, E. Farge, Mechanotransduction in tumor progression: The dark side of the force. *J. Cell Biol.* **217**, 1571–1587 (2018).
9. S. C. Wei, J. Yang, Forcing through tumor metastasis: The interplay between tissue rigidity and epithelial-mesenchymal transition. *Trends Cell Biol.* **26**, 111–120 (2016).
10. K. M. Shakya, A. Noyes, R. Kallin, R. E. Peltier, Evaluating the efficacy of cloth facemasks in reducing particulate matter exposure. *J. Expo. Sci. Environ. Epidemiol.* **27**, 352–357 (2017).
11. J. Bauer, M. A. B. Emon, J. J. Staudacher, A. L. Thomas, J. Zessner-Spitzenberg, G. Mancinelli, N. Krett, M. T. Saif, B. Jung, Increased stiffness of the tumor microenvironment in colon cancer stimulates cancer associated fibroblast-mediated prometastatic activin A signaling. *Sci. Rep.* **10**, 50 (2020).
12. D. Hanahan, L. M. Coussens, Accessories to the crime: Functions of cells recruited to the tumor microenvironment. *Cancer Cell* **21**, 309–322 (2012).
13. G. S. Karagiannis, T. Poutahidis, S. E. Erdman, R. Kirsch, R. H. Riddell, E. P. Diamandis, Cancer-associated fibroblasts drive the progression of metastasis through both paracrine and mechanical pressure on cancer tissue. *Mol. Cancer Res.* **10**, 1403–1418 (2012).
14. S. Kumar, V. M. Weaver, Mechanics, malignancy, and metastasis: The force journey of a tumor cell. *Cancer Metastasis Rev.* **28**, 113–127 (2009).
15. M. J. Bissell, H. G. Hall, G. Parry, How does the extracellular matrix direct gene expression? *J. Theor. Biol.* **99**, 31–68 (1982).
16. A. K. Harris, P. Wild, D. Stopak, Silicone rubber substrata: A new wrinkle in the study of cell locomotion. *Science* **208**, 177–179 (1980).
17. W. M. Leader, D. Stopak, A. K. Harris, Increased contractile strength and tightened adhesions to the substratum result from reverse transformation of CHO cells by dibutyryl cyclic adenosine monophosphate. *J. Cell Sci.* **64**, 1–11 (1983).
18. Y.-L. Wang, R. J. Pelham Jr., [39] Preparation of a flexible, porous polyacrylamide substrate for mechanical studies of cultured cells. *Methods Enzymol.* **298**, 489–496 (1998).
19. M. Dembo, Y.-L. Wang, Stresses at the cell-to-substrate interface during locomotion of fibroblasts. *Biophys. J.* **76**, 2307–2316 (1999).
20. M. Funaki, P. A. Janmey, in *Biology and Engineering of Stem Cell Niches* (Elsevier, 2017), pp. 363–373.
21. S. Munevar, Y. Wang, M. Dembo, Traction force microscopy of migrating normal and H-ras transformed 3T3 fibroblasts. *Biophys. J.* **80**, 1744–1757 (2001).
22. U. S. Schwarz, J. R. D. Soiné, Traction force microscopy on soft elastic substrates: A guide to recent computational advances. *Biochim. Biophys. Acta Mol. Cell Res.* **1853**, 3095–3104 (2015).
23. S. G. Knoll, M. Y. Ali, M. T. A. Saif, A novel method for localizing reporter fluorescent beads near the cell culture surface for traction force microscopy. *J. Vis. Exp.*, 51873 (2014).
24. J. L. Tan, J. Tien, D. M. Pirone, D. S. Gray, K. Bhadriraju, C. S. Chen, Cells lying on a bed of microneedles: An approach to isolate mechanical force. *Proc. Natl. Acad. Sci. U.S.A.* **100**, 1484–1489 (2003).

25. S. Ghassemi, G. Meacci, S. Liu, A. A. Gondarenko, A. Mathur, P. Roca-Cusachs, M. P. Sheetz, J. Hone, Cells test substrate rigidity by local contractions on submicrometer pillars. *Proc. Natl. Acad. Sci. U.S.A.* **109**, 5328–5333 (2012).
26. A. Saez, A. Buguin, P. Silberzan, B. Ladoux, Is the mechanical activity of epithelial cells controlled by deformations or forces? *Biophys. J.* **89**, L52–L54 (2005).
27. C. Grashoff, B. D. Hoffman, M. D. Brenner, R. Zhou, M. Parsons, M. T. Yang, M. A. McLean, S. G. Sligar, C. S. Chen, T. Ha, M. A. Schwartz, Measuring mechanical tension across vinculin reveals regulation of focal adhesion dynamics. *Nature* **466**, 263–266 (2010).
28. D. R. Stabley, C. Jurchenko, S. S. Marshall, K. S. Salaita, Visualizing mechanical tension across membrane receptors with a fluorescent sensor. *Nat. Methods* **9**, 64–67 (2012).
29. M. H. Jorrisch, W. Shih, S. Yamada, Myosin IIA deficient cells migrate efficiently despite reduced traction forces at cell periphery. *Biol. Open.* **2**, 368–372 (2013).
30. K. Duval, H. Grover, L.-H. Han, Y. Mou, A. F. Pegoraro, J. Fredberg, Z. Chen, Modeling physiological events in 2D vs. 3D cell culture. *Phys. Ther.* **32**, 266–277 (2017).
31. B. A. Nerger, M. J. Siedlik, C. M. Nelson, Microfabricated tissues for investigating traction forces involved in cell migration and tissue morphogenesis. *Cell. Mol. Life Sci.* **74**, 1819–1834 (2017).
32. D. A. Stout, E. Bar-Kochba, J. B. Estrada, J. Toyjanova, H. Kesari, J. S. Reichner, C. Franck, Mean deformation metrics for quantifying 3D cell–matrix interactions without requiring information about matrix material properties. *Proc. Natl. Acad. Sci. U.S.A.* **113**, 2898–2903 (2016).
33. J. Steinwachs, C. Metzner, K. Skodzek, N. Lang, I. Thievessen, C. Mark, S. Münster, K. E. Aifantis, B. Fabry, Three-dimensional force microscopy of cells in biopolymer networks. *Nat. Methods* **13**, 171–176 (2016).
34. W. R. Legant, A. Pathak, M. T. Yang, V. S. Deshpande, R. M. McMeeking, C. S. Chen, Microfabricated tissue gauges to measure and manipulate forces from 3D microtissues. *Proc. Natl. Acad. Sci. U.S.A.* **106**, 10097–10102 (2009).
35. K. R. Levental, H. Yu, L. Kass, J. N. Lakins, M. Egeblad, J. T. Erler, S. F. T. Fong, K. Csiszar, A. Giaccia, W. Weninger, M. Yamauchi, D. L. Gasser, V. M. Weaver, Matrix crosslinking forces tumor progression by enhancing integrin signaling. *Cell* **139**, 891–906 (2009).
36. M. C. Lampi, C. A. Reinhart-King, Targeting extracellular matrix stiffness to attenuate disease: From molecular mechanisms to clinical trials. *Sci. Transl. Med.* **10**, eaao0475 (2018).
37. J. Bauer, J. J. Staudacher, G. Mancinelli, N. Krett, E. Bashar, P. Grippo, M. T. A. Saif, B. Jung, in *Cancer Research* (American Association for Cancer Research, 2018), vol. 78, pp. 177–177.
38. M. P. Jacob, Extracellular matrix remodeling and matrix metalloproteinases in the vascular wall during aging and in pathological conditions. *Biomed. Pharmacother.* **57**, 195–202 (2003).
39. K. T. Weber, Extracellular matrix remodeling in heart failure: A role for de novo angiotensin II generation. *Circulation* **96**, 4065–4082 (1997).
40. T. R. Cox, D. Bird, A. M. Baker, H. E. Barker, M. W.-Y. Ho, G. Lang, J. T. Erler, LOX-mediated collagen crosslinking is responsible for fibrosis-enhanced metastasis. *Cancer Res.* **73**, 1721–1732 (2013).
41. T. R. Cox, J. T. Erler, Remodeling and homeostasis of the extracellular matrix: Implications for fibrotic diseases and cancer. *Dis. Model. Mech.* **4**, 165–178 (2011).
42. A. S. Barrett, thesis, University of Colorado (2010).
43. G.-F. Xiong, R. Xu, Function of cancer cell-derived extracellular matrix in tumor progression. *J. Cancer Metastasis Treat.* **2**, 357–364 (2016).
44. S. G. Knoll, M. T. A. Saif, Light induced, localized, and abrupt force relaxations in fibroblast cells on soft substrates. *Extrem. Mech. Lett.* **8**, 257–265 (2016).
45. M. A. B. Emon, S. Knoll, U. Doha, D. Baietto, L. Ladehoff, M. Sivaguru, M. T. A. Saif, Threshold illumination for non-invasive imaging of cells and tissues. bioRxiv 2020.01.16.909911 [**Preprint**] (2020).
46. F. A. Osorio, E. Bilbao, R. Bustos, F. Alvarez, Effects of concentration, bloom degree, and ph on gelatin melting and gelling temperatures using small amplitude oscillatory rheology. *Int. J. Food Prop.* **10**, 841–851 (2007).
47. O. Aydin, X. Zhang, S. Nuethong, G. J. Pagan-Diaz, R. Bashir, M. Gazzola, M. T. A. Saif, Neuromuscular actuation of biohybrid motile bots. *Proc. Natl. Acad. Sci. U.S.A.* **116**, 19841–19847 (2019).
48. D. Wiltz, C. Alexander Arevalos, L. R. Balaoing, A. A. Blancas, M. C. Sapp, X. Zhang, K. Jane Grande-Allen, *Calcific Aortic Valve Disease* (InTech, 2013).
49. M. Achilli, D. Mantovani, Tailoring mechanical properties of collagen-based scaffolds for vascular tissue engineering: The effects of pH, temperature and ionic strength on gelation. *Polymers* **2**, 664–680 (2010).
50. C. A. Schneider, W. S. Rasband, K. W. Eliceiri, NIH Image to ImageJ: 25 years of image analysis. *Nat. Methods* **9**, 671–675 (2012).
51. M. Elhebeary, M. A. B. Emon, O. Aydin, M. T. A. Saif, A novel technique for *in situ* uniaxial tests of self-assembled soft biomaterials. *Lab Chip* **19**, 1153–1161 (2019).
52. H. W. Schreier, M. A. Sutton, Systematic errors in digital image correlation due to undermatched subset shape functions. *Exp. Mech.* **42**, 303–310 (2002).
53. A. Marinkovi'c, J. D. Mih, J.-A. Park, F. Liu, D. J. Tschumperlin, Improved throughput traction microscopy reveals pivotal role for matrix stiffness in fibroblast contractility and TGF-β responsiveness. *Am. J. Physiol. Lung Cell. Mol. Physiol.* **303**, 169–180 (2012).
54. Z. Messi, A. Bornert, F. Raynaud, A. B. Verkhovsky, Traction forces control cell-edge dynamics and mediate distance sensitivity during cell polarization. *Curr. Biol.* **30**, 1762–1769.e5 (2020).
55. A. J. Licup, S. Münster, A. Sharma, M. Sheinman, L. M. Jawerth, B. Fabry, D. A. Weitz, F. C. MacKintosh, Stress controls the mechanics of collagen networks. *Proc. Natl. Acad. Sci. U.S.A.* **112**, 9573–9578 (2015).
56. B. A. Roeder, K. Kokini, J. E. Sturgis, J. P. Robinson, S. L. Voytik-Harbin, Tensile mechanical properties of three-dimensional type I collagen extracellular matrices with varied microstructure. *J. Biomech. Eng.* **124**, 214–222 (2002).
57. C. Storm, J. J. Pastore, F. C. MacKintosh, T. C. Lubensky, P. A. Janmey, Nonlinear elasticity in biological gels. *Nature* **435**, 191–194 (2005).
58. Y. Miki, K. Ono, S. Hata, T. Suzuki, H. Kumamoto, H. Sasano, The advantages of co-culture over mono cell culture in simulating *in vivo* environment. *J. Steroid Biochem. Mol. Biol.* **131**, 68–75 (2012).
59. M. Devarasetty, A. Dominijanni, S. Herberg, E. Shelkey, A. Skardal, S. Soker, Simulating the human colorectal cancer microenvironment in 3D tumor-stroma co-cultures *in vitro* and *in vivo*. *Sci. Rep.* **10**, 9832 (2020).
60. J. Rajagopalan, M. T. A. Saif, Fabrication of freestanding 1-D PDMS microstructures using capillary micromolding. *J. Microelectromech. Syst.* **22**, 992–994 (2013).
61. Corning Incorporated, Certificate of Analysis for Corning Collagen I High Concentration (HC), Rat Tail; https://certs-ecatalog.corning.com/life-sciences/certs/354249_9343002.pdf.
62. J. F. Ganghoffer, *Multiscale Biomechanics* (Elsevier, 2018).
63. J. Bergström, *Mechanics of Solid Polymers: Theory and Computational Modeling* (Elsevier, 2015).

Acknowledgments: We thank L. Yang for assistance with the A549 cells. **Funding:** Research reported in this publication was partially supported by the National Institute of Biomedical Imaging and Bioengineering of the NIH under award number T32EB019944 to B.E. The content is solely the responsibility of the authors and does not necessarily represent the official views of the NIH. Funding was also provided by NSF grant NSF ECCS 19-34991, Mayo Clinic grant PO 66236006, and Illinois Cancer Center seed grant, University of Illinois at Urbana-Champaign.
Author contributions: B.E. and M.T.A.S. conceived and designed the experiments. B.E. performed the experiments. B.E., Z.L., M.S.H.J., and U.D. performed imaging and analysis. B.E., Z.L., M.S.H.J., F.K., and M.T.A.S. prepared the manuscript. All authors have read and approved the final manuscript. **Competing interests:** The authors declare that they have no competing interests. **Data and materials availability:** All data needed to evaluate the conclusions in the paper are present in the paper and/or the Supplementary Materials. Additional data related to this paper may be requested from the authors.

Submitted 14 October 2020
Accepted 11 February 2021
Published 9 April 2021
10.1126/sciadv.abf2629

Citation: B. Emon, Z. Li, M. S. H. Joy, U. Doha, F. Kosari, M. T. A. Saif, A novel method for sensor-based quantification of single/multicellular force dynamics and stiffening in 3D matrices. *Sci. Adv.* **7**, eabf2629 (2021).

A novel method for sensor-based quantification of single/multicellular force dynamics and stiffening in 3D matrices

Bashar Emon, Zhengwei Li, Md Saddam H. Joy, Umnia Doha, Farhad Kosari and M. Taher A. Saif

Sci Adv **7** (15), eabf2629.
DOI: 10.1126/sciadv.abf2629